

Alternative configuration scheme for signal amplification with scanning ion conductance microscopy

Cite as: Rev. Sci. Instrum. **86**, 023706 (2015); <https://doi.org/10.1063/1.4907360>
Submitted: 18 November 2014 . Accepted: 15 January 2015 . Published Online: 18 February 2015

Joonhui Kim, Seong-Oh Kim, and Nam-Joon Cho 



View Online



Export Citation



CrossMark

ARTICLES YOU MAY BE INTERESTED IN

[Double micropipettes configuration method of scanning ion conductance microscopy](#)

Review of Scientific Instruments **87**, 073703 (2016); <https://doi.org/10.1063/1.4958643>

[Image formation, resolution, and height measurement in scanning ion conductance microscopy](#)

Journal of Applied Physics **105**, 094905 (2009); <https://doi.org/10.1063/1.3122007>

[Phase modulation mode of scanning ion conductance microscopy](#)

Applied Physics Letters **105**, 053113 (2014); <https://doi.org/10.1063/1.4891571>



Alternative configuration scheme for signal amplification with scanning ion conductance microscopy

Joonhui Kim,^{1,2} Seong-Oh Kim,^{1,2} and Nam-Joon Cho^{1,2,3,a)}

¹*School of Materials Science and Engineering, Nanyang Technological University, 50 Nanyang Avenue, 639798 Singapore*

²*Centre for Biomimetic Sensor Science, Nanyang Technological University, 50 Nanyang Drive, 637553 Singapore*

³*School of Chemical and Biomedical Engineering, Nanyang Technological University, 62 Nanyang Drive, 637459 Singapore*

(Received 18 November 2014; accepted 15 January 2015; published online 18 February 2015)

Scanning Ion Conductance Microscopy (SICM) is an emerging nanotechnology tool to investigate the morphology and charge transport properties of nanomaterials, including soft matter. SICM uses an electrolyte filled nanopipette as a scanning probe and detects current changes based on the distance between the nanopipette apex and the target sample in an electrolyte solution. In conventional SICM, the pipette sensor is excited by applying voltage as it raster scans near the surface. There have been attempts to improve upon raster scanning because it can induce collisions between the pipette sidewalls and target sample, especially for soft, dynamic materials (e.g., biological cells). Recently, Novak *et al.* demonstrated that hopping probe ion conductance microscopy (HPICM) with an adaptive scan method can improve the image quality obtained by SICM for such materials. However, HPICM is inherently slower than conventional raster scanning. In order to optimize both image quality and scanning speed, we report the development of an alternative configuration scheme for SICM signal amplification that is based on applying current to the nanopipette. This scheme overcomes traditional challenges associated with low bandwidth requirements of conventional SICM. Using our alternative scheme, we demonstrate successful imaging of L929 fibroblast cells and discuss the capabilities of this instrument configuration for future applications. © 2015 Author(s). All article content, except where otherwise noted, is licensed under a Creative Commons Attribution 3.0 Unported License. [<http://dx.doi.org/10.1063/1.4907360>]

I. INTRODUCTION

Over the past few decades, many techniques have been developed based on the Scanning Probe Microscopy (SPM) principle in order to understand molecular-level biological phenomena by measuring the interaction between a nanoscale probe and the sample surface. Thus far, the Atomic Force Microscope (AFM) is the most popular SPM technique for investigating cell morphology and molecular interaction forces.¹⁻³ However, even in the less intrusive, “non-contact” tapping mode, the AFM cantilever oscillates at amplitudes above the sub-nanometer scale and causes its probe tip to continuously contact the sample, which disturbs soft biological samples.⁴⁻⁷

While most SPM techniques were originally designed for imaging nanomaterials in vacuum or air conditions, the scanning ion conductance microscope (SICM), which was invented by Paul Hansma in 1989,⁸ is unique because it was designed to probe soft biological systems. In order to do so, the SICM utilizes ion current as the signal in order to measure the topography of soft non-conducting samples. In addition to its role as an imaging tool, SICM has also demonstrated utility as

a multi-functional tool for single channel patch-clamping,^{9,10} surface patterning or drug delivery,¹¹⁻¹⁶ combined scanning electrochemical microscopy,^{17,18} and measuring mechanical properties.¹⁹⁻²¹

An electrolyte-filled nanopipette, which is pulled from a glass capillary, is used as the probe.⁸ Two electrodes, a pipette electrode which is inside the pipette, and a bath electrode, which is located on the outside of the pipette, are used to detect ion conductance changes based on the distance between the pipette apex and the sample surface. As the nanopipette tip reaches near to the surface of the sample, the gap through which ions flow is impeded, causing the ion current to decrease. In the earliest convention, the nanopipette was raster scanned across the surface while a feedback loop adjusts the vertical position in order to keep the ion conductance constant by adjusting the nanopipette tip height, enabling the topography of the surface to be mapped with high resolution.⁸

As the SICM technique became popular, different modes were introduced. Those modes include the direct current (DC),^{8,22} alternate current (AC),²³⁻²⁵ and hopping modes.²⁶⁻²⁸ DC mode was first utilized to demonstrate live cell imaging as it maintains a constant direct current on the sample surface during raster scanning. Since the direct current maintains the tip-sample distance while the scanning probe follows the lateral topography, it has an inherent limitation for scanning

^{a)}Author to whom correspondence should be addressed. Electronic mail: njcho@ntu.edu.sg

larger or coarse objects.²⁴ In order to improve sensitivity and stability, AC mode was introduced by the superimposition of the DC signal with a current component.²³ It operates similarly to tapping mode in AFM by modulating the pipette along the z-axis within few tens of nanometers, and detects the amplitude signal using a lock-in amplifier.^{23–25} Despite stable scanning of the sample topography, in AC mode, the pipette can only detect the distance signal at the pipette apex and is, hence, not suitable for investigating the large morphological variations inherent on cell surfaces.²⁹

In order to circumvent the aforementioned challenges with SICM imaging, the hopping probe ion conductance microscope (HPICM) was introduced enabling the scanning probe to be retracted after each positional recording.^{26–28} In this mode, the probe approaches the sample until reaching the given setpoint vertically and records the distance from the initial z-position, returns to the initial z-position, and then laterally moves to the next position. Possible interference of coarse or fluctuating morphology is minimized using this non-continuous scan approach. However, the advantages of this mode were initially offset by the requirement for an appreciably longer equivalent scan time due to the greater travel distance of the pipette. To improve imaging speed in HPICM mode, Novak *et al.*²⁹ introduced an adaptive algorithm based on a low resolution prescan of the entire sample followed by more detailed imaging of regions that demand higher resolution analysis. With a maturing SICM instrumentation field, there have hitherto been many successful demonstrations of various modes adapted to the demands of particular applications. At the same time, all of these modes are fundamentally based on a voltage source, which means applying a constant voltage between the pipette electrode and the bath electrode and detecting changes in current flow through the nanopipette.

Herein, we introduce an alternative configuration scheme for SICM measurements based on a current source, in which a constant current is applied from the pipette electrode to the bath electrode and detect changes in the voltage associated with the nanopipette. Based on the current source design, the fabrication of a prototype printed circuit board (PCB) configuration is reported, which is compatible with a commercial SICM instrument. Analysis of the frequency response and noise spectrum of the current source shows better performance than the conventional voltage source. A microfabricated polydimethylsiloxane (PDMS) grating sample and the biological cell are imaged in the current source configuration scheme, and the results are compared with those obtained by a conventional, voltage source. Possible applications of this new configuration scheme are discussed.

II. OPERATING PRINCIPLE OF SICM BASED ON VOLTAGE SOURCE AND ITS LIMITATION

The conventional SICM circuit uses a voltage source to excite the system comprised of the pipette electrode, the electrolyte solution, and the bath electrode. This configuration can be divided and modeled as three resistances, the pipette resistance R_P , the access resistance R_{AC} , and the solution resistance R_S as shown in Figure 1. The pipette resistance R_P

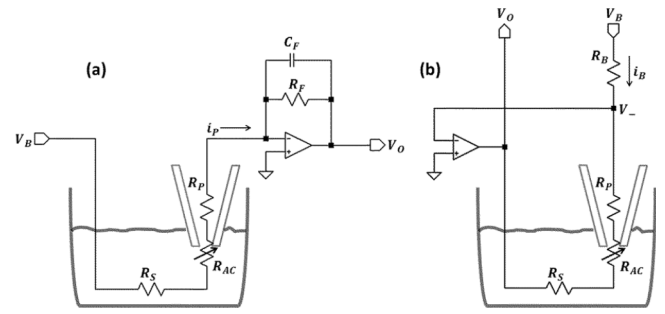


FIG. 1. Principle of the SICM signal amplification. The SICM pipette consists of the pipette resistance R_P and the access resistance R_{AC} , which varies corresponding to the distance between the pipette apex and the sample surface and the solution resistance R_S . (a) The conventional voltage source configuration. When voltage bias V_B is applied to the pipette, current i_P is generated. The amplifier converts i_P to voltage V_O with transimpedance gain R_F . (b) Alternative configuration scheme for signal amplification and the current source configuration. An alternative configuration applies current i_B to the pipette and detects voltage drop V_O .

represents the resistance inside of the pipette, and R_P is the resistance when the pipette is far from the sample surface. The cross-section of the pipette end is small and tapered so the pipette resistance typically reaches over 100 M Ω . The access resistance R_{AC} varies depending on the distance between the pipette apex and the sample surface. R_{AC} is zero when the pipette is far from the sample surface and increases when the pipette becomes closer to the sample surface because the area of the ion current path between the pipette and the surface is decreased. In most imaging conditions with the setpoint at 1%~2% of R_P , the access resistance R_{AC} only contributes a small portion to the total pipette resistance. For mathematical convention, the access resistance can be simplified by

$$R_{AC} = R_P \delta(z), \quad (1)$$

where $\delta(z)$ is the dependent term of the distance between the pipette and the sample surface. The solution resistance R_S represents the bulk resistance from the access resistance to the bath electrode, but compared to the pipette resistance the solution resistance is negligible. Hence, the total resistance R_T between two electrodes can be expressed by

$$R_T = R_P + R_{AC} + R_S \cong R_P (1 + \delta(z)). \quad (2)$$

When applying a constant voltage between two electrodes using a voltage source, the current i_P is generated and its value changes based on the distance between the pipette and the sample as follows:

$$i_P = \frac{V_B}{R_T} = \frac{V_B}{R_P (1 + \delta(z))}. \quad (3)$$

In order to convert the generated current i_P into the voltage, a transimpedance amplifier is used. The converted voltage of the current i_P is proportional to the feedback resistance R_F ,

$$V_O = R_F \cdot i_P. \quad (4)$$

The thermal noise of this transimpedance amplifier is characterized by $\sqrt{4kT \cdot R_F \cdot BW}$, where $k = 1.38 \times 10^{-23}$ J/K is Boltzmann's constant, T is absolute temperature and BW is the bandwidth of interest. Considering the signal

to noise ratio (SNR) of the transimpedance amplifier, the feedback resistance should be set at significantly higher values because the current gain is linearly proportional to R_F and the noise is proportional to $\sqrt{R_F}$. In this case, the SNR improves proportionally to $\sqrt{R_F}$. However, in actuality, the resistor R_F has a stray capacitance C_F which is on the order of 0.1 pF in parallel. Therefore, the output voltage is dependent on the frequency and low pass-filtered with the bandwidth $f_0 = 1/2\pi R_F C_F$, which is mathematically expressed by

$$V_O(f) = R_F \cdot i_P \cdot \frac{1}{1 + j \cdot f/f_0}, \quad (5)$$

where $j = \sqrt{-1}$ is imaginary number and f is frequency. As such, it is not practical to set R_F too high because the high frequency signal is eliminated by the low-pass filtering.

This conventional voltage source configuration has a tradeoff between the SNR and the bandwidth. If R_F is set at a higher value to get a higher SNR, the bandwidth is reduced. On the other hand, in order to get a higher bandwidth, the SNR is poorer. To balance the SNR and proper bandwidth, we set the R_F at 1 G Ω in order to obtain a bandwidth of around 1 kHz for SICM measurements using the voltage source configuration in this work. In order to circumvent this tradeoff between SNR and bandwidth, we note that an alternate preamplifier circuit is required.

III. ALTERNATE SIGNAL AMPLIFICATION CONFIGURATION BASED ON CURRENT SOURCE AND ITS CHARACTERISTICS

The alternate circuit uses a current source to apply a constant current i_B from the pipette electrode to the bath electrode and to detect the voltage changes between two electrodes as shown in Figure 1(b). When negative feedback of an operational amplifier (opamp) works, the two input nodes, inverting input (-), and non-inverting input (+) of the opamp become the same voltage, or the voltage of the inverting input node of opamp, V_- is virtually ground or 0 V, and the biasing current is determined by

$$i_B = \frac{V_B}{R_B}. \quad (6)$$

The bias current i_B passes through two electrodes, the voltage drops the amount of total resistance R_T , and the output voltage is

$$V_O = -R_T \cdot i_B = -R_P(1 + \delta(z)) \cdot i_B. \quad (7)$$

In contrast to the voltage source, the output voltage is independent from the circuit element because the applied voltage V_B and current i_B are constant during the operation. In other words, the bandwidth is not limited by circuit components when applying current to the pipette.

In addition, using a current source, the overall impedance of the circuit can be reduced. The output noise voltage of voltage source configuration, e_V , and current source configuration, e_I , are expressed by

$$e_V = \left(1 + \frac{R_F}{R_T}\right) \sqrt{4kT \cdot (R_T \parallel R_F) \cdot BW}, \quad (8)$$

$$e_I = \left(1 + \frac{R_T}{R_B}\right) \sqrt{4kT \cdot (R_T \parallel R_B) \cdot BW}, \quad (9)$$

where \parallel is parallel resistance of the two resistors, $(R_1 \parallel R_2) = R_1 R_2 / (R_1 + R_2)$. The parallel resistance $(R_1 \parallel R_2)$ is less than R_1 and R_2 . As there is no opportunity to adjust the pipette resistance R_P , the minimum value of $(R_T \parallel R_F)$ is R_T when R_F is infinite. In the case of the current source, we can set R_B to be smaller than R_T , and the output noise can be decreased independently from the pipette resistance.

We also consider the applied power between two electrodes. The applied power in the current source configuration is proportional to the total resistance, $P = I_B^2 \cdot R_T$, whereas the applied power in the voltage source configuration is inversely proportional to the total resistance, $P = V_B^2 / R_T$. In the extreme case, when the pipette is broken during imaging, and the pipette resistance is reduced suddenly, the current source configuration automatically reduces the power between the two electrodes. This feature would be helpful to image living cell to avoid unnecessary electrical stimulus to cells in the worst case.

The implementation of the current source configuration is shown in Figure 2. To interconnect the external voltage source, a differential amplifier was used for eliminating ground loop noise (panel A). The voltage controlled current source was designed with the FET input amplifier, AD8067 (Analog Devices, Inc., MA, USA). This amplifier has a low input bias current, typically 1.0 pA, and has a wide gain bandwidth product (GBP), 200 MHz. Difet[®] input amplifiers, OPA128 and OPA129 (Texas Instruments, Inc., TX, USA), can be used instead of AD8067. We set the bias resistor R_B to 10 M Ω in order to reduce the significance of the input offset voltage (AD8067 has 1 mV offset voltage in maximum), in comparison to the bias voltage V_B which is around 10 ~ 100 mV. Subminiature version A (SMA) connectors and cables were used to shield high impedance nodes from the pipette distance sensing system. In principle, it is better to connect the output of the opamp (port 3) to the bath electrode in order to block external noise because the electrolyte solution, which has a relatively lower impedance than the pipette resistance, might behave like a shield. The instrumentation amplifier INA116 (Texas Instruments, Inc., TX, USA) was employed to detect the voltage difference between the non-inverting input and the inverting input of the FET input amplifier. Finally, the signal passed to the output through a 10 kHz 2nd order Bessel filter (port 4) for noise measurement and imaging, and the signal passed via the follower (port 5) for bandwidth measurement. Opamps for the low pass filter and others consisted of OPA2209 (Texas Instruments, Inc., TX, USA).

In order to test the alternative current source configuration, the noise and bandwidth of the two modes were performed with a resistor of 100 M Ω . The noise voltage spectral density is plotted in Figure 3(b). This was measured by a data acquisition board, NI PCI-6251 (National Instruments Corp., TX, USA), and data were recorded for 10 s with 200 kilo-samples per seconds (kSPS) after 10 kHz low-pass filter to prevent an aliasing effect and analyzed by a one-side power spectrum density. The noise spectral densities

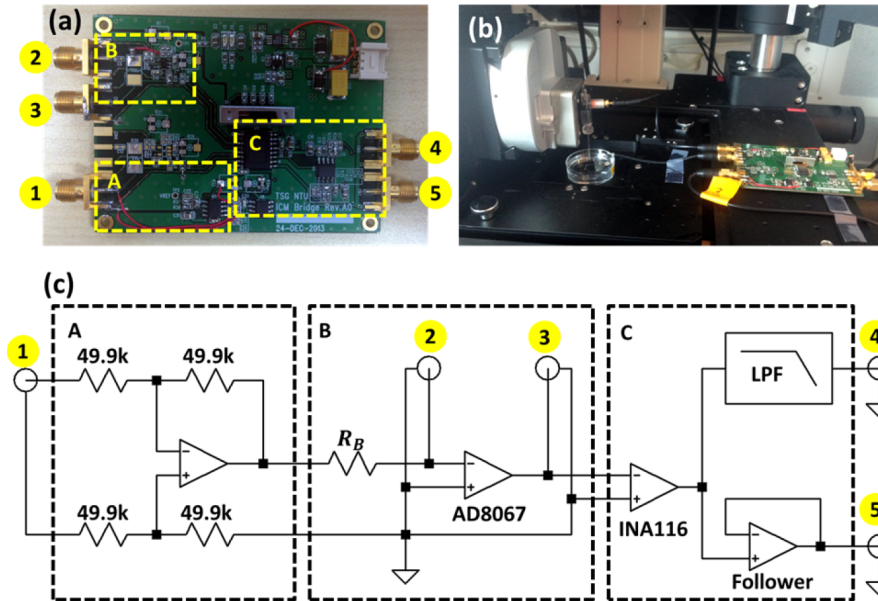


FIG. 2. (a) The PCB for the current source configuration. (b) Experimental setup for current bias signal amplification mode. (c) Detailed schematic of the PCB. The external bias is connected to port 1; the pipette electrode and the bath electrode are connected to ports 2 and 3, respectively. Ports 4 and 5 are to monitor output voltage with and without low-pass filtering, respectively. Dotted panel A is for avoiding ground loop noise and dotted panel B is the main circuit of current bias signal amplification mode. Dotted panel C indicates additional signal conditioning for output filter and buffer.

at 1 kHz are $15.7 \mu\text{V}/\sqrt{\text{Hz}}$ and $5.38 \mu\text{V}/\sqrt{\text{Hz}}$ for the voltage source and current source configurations, respectively. These values correspond well with the calculated thermal noise at 25°C , $13.5 \mu\text{V}/\sqrt{\text{Hz}}$ and $4.26 \mu\text{V}/\sqrt{\text{Hz}}$ for the voltage source

and current source configurations, respectively. The thermal noise from the current source configuration can easily be smaller than the thermal noise of R_P , the latter of which is $14.1 \mu\text{V}/\sqrt{\text{Hz}}$ in the $100 \text{ M}\Omega$ case. The frequency responses of both configurations are shown in Figure 3(a), which were taken using a lock-in amplifier, SR830 (Stanford Research System, Inc., CA, USA). The bandwidth of the voltage source configuration with $1 \text{ G}\Omega$ feedback resistor is 1.69 kHz as expected, and the bandwidth of current source configuration is 13.2 kHz which is much higher than the voltage source configuration.

IV. COMPARISON OF IMAGE QUALITY

As discussed above, the noise and bandwidth signals of the current source configuration show improved performance compared to the voltage source configuration. In order to determine if a similar performance improvement can be realized in actual imaging conditions, we attempted to image two samples in different SICM modes: a grating sample in DC-mode and a L929 fibroblast cell in hopping mode. A commercial SICM, NX-Bio (Park Systems Corp., Suwon, Korea) was used as the SICM imaging platform. The nanopipette was fabricated from borosilicate capillaries which have 0.6 mm inner diameter and 1.0 mm outer diameter (Narishige, Tokyo, Japan) by using a CO_2 -laser-based micropipette puller, Model P-2000 (Sutter Instruments, CA, USA).

Before the imaging test, the current-distance curve of the voltage source and the voltage-distance curve of the current source configuration were investigated as shown in Figures 4(a) and 4(d). The output of the voltage source configuration represents the conductance between the pipette and the bath electrodes, which can be interpreted as current. The output of the current source configuration represents the

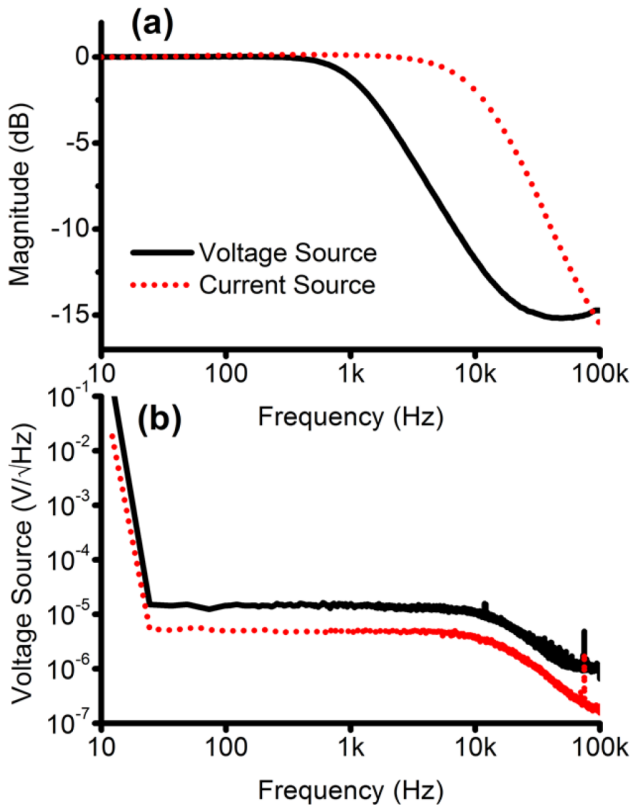


FIG. 3. (a) Comparison of magnitude (dB) of two different signal amplification modes as a function of frequency (Hz). (b) Comparison of noise spectral density fixed at a resistance of $100 \text{ M}\Omega$ for two different signal amplification modes. Black solid is for voltage source and red dotted is for current source configuration.

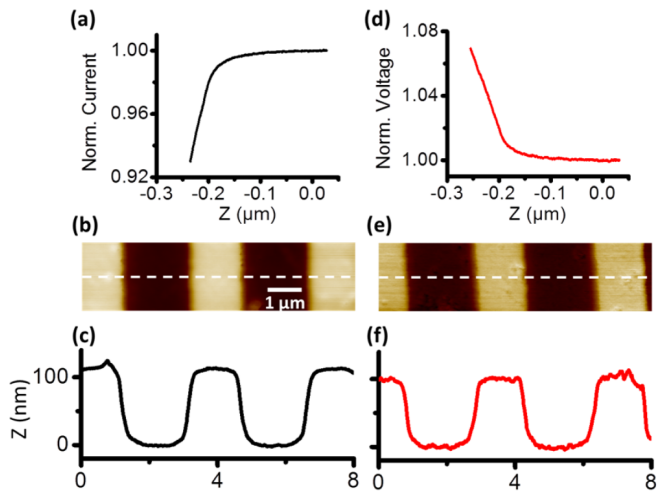


FIG. 4. Comparison of SICM imaging in voltage source and current source configurations. (a) Current-distance curve for voltage source configuration. (b) $8 \mu\text{m}$ by $2 \mu\text{m}$ standard PDMS grating image of voltage source in DC-mode and (c) line profile of dashed-line (white) from the image. (d) Voltage-distance curve of current source configuration and (e) corresponding standard PDMS grating image and (f) line profile.

resistance between the two electrodes. The normalized output of the current source configuration increases when the pipette approaches the surface (Fig. 4(d)) which is in contrast to the decreasing output of the voltage source configuration (Fig. 4(a)). The polarity of the feedback should be negated due to the polarity of the error signal, which is the difference between the setpoint and measured output voltage, $e = (\text{measured}) - (\text{setpoint})$, is reversed in the current source configuration.

For example, when the error signal is a positive value, the pipette moves to the surface in the voltage source configuration, whereas the pipette moves far from the surface in the current source configuration with the same control software. As such, we modified the feedback software in order to calculate the proper error signal for the current source configuration.

DC-mode SICM images of a grating sample are presented in Figures 4(b) and 4(e), and the corresponding line profile is shown in Figures 4(c) and 4(f). The sample was prepared on PDMS by stamping of a $3.5 \mu\text{m}$ pitch and 118.5 nm height sample. The image and line profile obtained using a current source (Figs. 4(e) and 4(f)) display sharper details than the image obtained using a voltage source.

Furthermore, to demonstrate the utility of the alternative current source configuration on soft biological samples, we obtained L929 fibroblast cell images (Figure 5). The cells were maintained in Dulbecco's Modified Eagle Medium (DMEM; Life Technique, Invitrogen USA) supplemented with 10% fetal bovine serum (FBS; Hyclone, Thermo) and 1% penicillin/ streptomycin (Gibco) at 37°C in a humidified atmosphere containing 5% CO_2 . The cells were harvested after trypsinization, washed, and re-suspended at 1×10^5 cells/ml concentrations in normal growth medium for subculture. A 1 ml aliquot of the cells containing medium was seeded on the experimental petri dish at a concentration of $1 \times 10^3 \text{ ml}^{-1}$. After 3 days culture, the cells were washed by Phosphate Buffered Saline (PBS) buffer 3 times and then treated with 4% paraformaldehyde (PFA) solution for 5 min. Before imaging, the fixed cells were washed again two times with PBS buffer.

For direct comparison, we scanned the cell surface using hopping mode with a 1.5% setpoint in order to compare

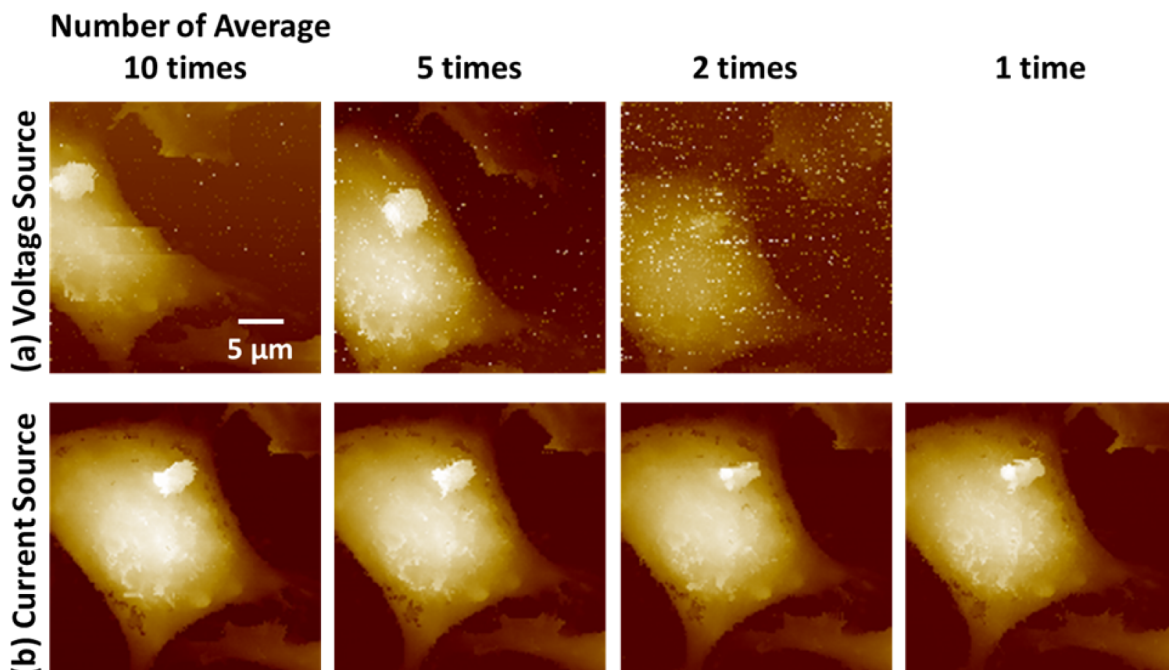


FIG. 5. Comparison of SICM cell imaging for two different configurations, conventional voltage source configuration, and modified current source configuration. (a) Using voltage source configuration, L929 cells were imaged with a varied number of digital average filters (average scan time) in order to compare image quality. The dots stand for noise due to low digital average filters. (b) Direct comparison of L929 cells images by modified current source configuration. In current source configuration, we are able to image with one time scan and presented consistent image resolution independent of the number of average scans. The scale bar represents $5 \mu\text{m}$.

between the voltage source and current source configurations. The control software stops the approach and records the height when the output voltage of the amplifier reaches the setpoint or $e \leq 0$. With a high noisy signal, the control software might stop before reaching the right setpoint value because the control software picks the noise, and the software records the height which is higher than the sample surface; this point is displayed as a white dot. In order to reduce noise, a digital average filter is used and the number of digital averages is related to the time duration for imaging. In the voltage source configuration, in order to acquire a relatively high resolution cell image, more than five average filters are required, as shown in Figure 5(a). Of note, there is noise (represented as white dots) two-times averaging and an image could not be obtained without a digital filter (one-time averaging). In marked contrast, using the current source configuration, we are able to scan and acquire reasonable cell images without digital filter. This finding demonstrates that the current source configuration might provide better performance than the voltage source configuration for imaging biological samples, and should be further explored.

V. CONCLUSION AND OUTLOOK

We have suggested an alternate method to operate the SICM which applies current to the pipette sensor instead of voltage. This current source configuration of the electric circuit can have a lower output noise and the bandwidth is not limited by the circuit component. We have successfully demonstrated DC-mode and hopping-mode images with faster acquisition time in same image quality. We believe that this improvement would be useful to investigate the nano-scale dynamics of living cells. Furthermore, a good aspect of the current source configuration is detecting the change of resistance linearly, and it can be helpful to analyze the behavior of the pipette dynamics more intuitively.

ACKNOWLEDGMENTS

This work was supported by the National Research Foundation (NRF-NRFF2011-01) and the National Medical Research Council (NMRC/CBRG/0005/2012).

¹D. P. Allison, N. P. Mortensen, C. J. Sullivan, and M. J. Doktycz, "Atomic force microscopy of biological samples," *Wiley Interdiscip. Rev.: Nanomed. Nanobiotechnol.* **2**(6), 618–634 (2010).

²Z. Shao, J. Yang, and A. P. Somlyo, "Biological atomic force microscopy: From microns to nanometers and beyond," *Annu. Rev. Cell Dev. Biol.* **11**(1), 241–265 (1995).

³E. Henderson, "Imaging of living cells by atomic force microscopy," *Prog. Surf. Sci.* **46**(1), 39–60 (1994).

⁴H. X. You, J. M. Lau, S. Zhang, and L. Yu., "Atomic force microscopy imaging of living cells: A preliminary study of the disruptive effect of the cantilever tip on cell morphology," *Ultramicroscopy* **82**(1), 297–305 (2000).

⁵J. Rheinlaender, N. A. Geisse, R. Proksch, and T. E. Schäffer, "Comparison of scanning ion conductance microscopy with atomic force microscopy for cell imaging," *Langmuir* **27**(2), 697–704 (2010).

⁶T. Ushiki, M. Nakajima, M. Choi, S.-J. Cho, and F. Iwata, "Scanning ion conductance microscopy for imaging biological samples in liquid: A

comparative study with atomic force microscopy and scanning electron microscopy," *Micron* **43**(12), 1390–1398 (2012).

⁷F. Anariba, J. H. Anh, G.-E. Jung, N.-J. Cho, and S.-J. Cho, "Biophysical applications of scanning ion conductance microscopy (SICM)," *Mod. Phys. Lett. B* **26**(05), 1130003 (2012).

⁸P. Hansma, B. Drake, O. Marti, S. Gould, and C. Prater, "The scanning ion-conductance microscope," *Science* **243**(4891), 641–643 (1989).

⁹J. Gorelik *et al.*, "Ion channels in small cells and subcellular structures can be studied with a smart patch-clamp system," *Biophys. J.* **83**(6), 3296–3303 (2002).

¹⁰P. Novak *et al.*, "Nanoscale-targeted patch-clamp recordings of functional presynaptic ion channels," *Neuron* **79**(6), 1067–1077 (2013).

¹¹A. Bruckbauer *et al.*, "Writing with DNA and protein using a nanopipette for controlled delivery," *J. Am. Chem. Soc.* **124**(30), 8810–8811 (2002).

¹²A. Bruckbauer *et al.*, "Multicomponent submicron features of biomolecules created by voltage controlled deposition from a nanopipette," *J. Am. Chem. Soc.* **125**(32), 9834–9839 (2003).

¹³K. T. Rodolfa, A. Bruckbauer, D. Zhou, Y. E. Korchev, and D. Klenerman, "Two-component graded deposition of biomolecules with a double-barreled nanopipette," *Angew. Chem.* **117**(42), 7014–7019 (2005).

¹⁴K. T. Rodolfa *et al.*, "Nanoscale pipetting for controlled chemistry in small arrayed water droplets using a double-barrel pipet," *Nano Lett.* **6**(2), 252–257 (2006).

¹⁵R. Adam Seger *et al.*, "Voltage controlled nano-injection system for single-cell surgery," *Nanoscale* **4**(19), 5843–5846 (2012).

¹⁶B. Babakinejad *et al.*, "Local delivery of molecules from a nanopipette for quantitative receptor mapping on live cells," *Anal. Chem.* **85**(19), 9333–9342 (2013).

¹⁷D. J. Comstock, J. W. Elam, M. J. Pellin, and M. C. Hersam, "Integrated ultramicroelectrode-nanopipette probe for concurrent scanning electrochemical microscopy and scanning ion conductance microscopy," *Anal. Chem.* **82**(4), 1270–1276 (2010).

¹⁸Y. Takahashi *et al.*, "Topographical and electrochemical nanoscale imaging of living cells using voltage-switching mode scanning electrochemical microscopy," *Proc. Natl. Acad. Sci. U. S. A.* **109**(29), 11540–11545 (2012).

¹⁹D. Sánchez *et al.*, "Noncontact measurement of the local mechanical properties of living cells using pressure applied via a pipette," *Biophys. J.* **95**(6), 3017–3027 (2008).

²⁰Y. Mizutani, M.-H. Choi, S.-J. Cho, and T. Okajima, "Nanoscale fluctuations on epithelial cell surfaces investigated by scanning ion conductance microscopy," *Appl. Phys. Lett.* **102**(17), 173703 (2013).

²¹J. Rheinlaender and T. E. Schäffer, "Mapping the mechanical stiffness of live cells with the scanning ion conductance microscope," *Soft Matter* **9**(12), 3230–3236 (2013).

²²Y. E. Korchev, C. L. Bashford, M. Milovanovic, I. Vodyanoy, and M. J. Lab, "Scanning ion conductance microscopy of living cells," *Biophys. J.* **73**(2), 653–658 (1997).

²³R. Proksch, R. Lal, P. K. Hansma, D. Morse, and G. Stucky, "Imaging the internal and external pore structure of membranes in fluid: Tapping-Mode scanning ion conductance microscopy," *Biophys. J.* **71**(4), 2155–2157 (1996).

²⁴D. Pastré, H. Iwamoto, J. Liu, G. Szabo, and Z. Shao, "Characterization of AC mode scanning ion-conductance microscopy," *Ultramicroscopy* **90**(1), 13–19 (2001).

²⁵A. I. Shevchuk *et al.*, "Simultaneous measurement of Ca^{2+} and cellular dynamics: Combined scanning ion conductance and optical microscopy to study contracting cardiac myocytes," *Biophys. J.* **81**(3), 1759–1764 (2001).

²⁶S. Mann, G. Hoffmann, A. Hengstenberg, W. Schuhmann, and I. Dietzel, "Pulse-mode scanning ion conductance microscopy—a method to investigate cultured hippocampal cells," *J. Neurosci. Methods* **116**(2), 113–117 (2002).

²⁷P. Happel and I. D. Dietzelm, "Backstep scanning ion conductance microscopy as a tool for long term investigation of single living cells," *J. Nanobiotechnol.* **7**(7), 7 (2009).

²⁸Y. Takahashi *et al.*, "Topographic imaging of convoluted surface of live cells by scanning ion conductance microscopy in a standing approach mode," *Phys. Chem. Chem. Phys.* **12**(34), 10012–10017 (2010).

²⁹P. Novak *et al.*, "Nanoscale live-cell imaging using hopping probe ion conductance microscopy," *Nat. Methods* **6**(4), 279–281 (2009).